Key Points:

- Precipitation extremes are enhanced by about 30%–40% in optimal and superoptimal squall lines compared to random convection
- The enhancement of extremes is due to reduced dilution by entrainment and enhanced initial vertical velocity of updrafts in optimal and superoptimal regimes
- The enhanced vertical velocity in convective updrafts does not depend on the orientation of squall lines in the superoptimal regime

Author Contributions:
Conceptualization: Sophie Abramian, Caroline Muller, Camille Risi
Formal analysis: Sophie Abramian
Funding acquisition: Caroline Muller

Extreme Precipitation in Tropical Squall Lines

Sophie Abramian[1] , Caroline Muller[2], and Camille Risi[1]

[1]Laboratoire de Météorologie Dynamique, IPSL, CNRS, Ecole Normale Supérieure, Sorbonne Université, PSL Research University, Paris, France, [2]Institute of Science and Technology Austria (ISTA), Klosterneuburg, Austria

Abstract Squall lines are substantially influenced by the interaction of low-level shear with cold pools associated with convective downdrafts. Beyond an optimal shear amplitude, squall lines tend to orient themselves at an angle with respect to the low-level shear. While the mechanisms behind squall line orientation seem to be increasingly well understood, uncertainties remain on the implications of this orientation. Roca and Fiolleau (2020, https://doi.org/10.1038/s43247-020-00015-4) show that long lived mesoscale convective systems, including squall lines, are disproportionately involved in rainfall extremes in the tropics. This article investigates the influence of the interaction between low-level shear and squall line outflow on squall line generated precipitation extrema in the tropics. Using a cloud resolving model, simulated squall lines in radiative convective equilibrium amid a shear-dominated regime (super optimal), a balanced regime (optimal), and an outflow dominated regime (suboptimal). Our results show that precipitation extremes in squall lines are 40% more intense in the case of optimal shear and remain 30% superior in the superoptimal regime relative to a disorganized case. With a theoretical scaling of precipitation extremes (C. Muller & Takayabu, 2020, https://doi.org/10.1088/1748-9326/ab7130), we show that the condensation rates control the amplification of precipitation extremes in tropical squall lines, mainly due to its change in vertical mass flux (dynamic component). The reduction of dilution by entrainment explains half of this change, consistent with Mulholland et al. (2021, https://doi.org/10.1175/jas-d-20-0299.1). The other half is explained by increased cloud-base velocity intensity in optimal and superoptimal squall lines.

Plain Language Summary Squall lines are bands of clouds and thunderstorms spanning hundreds of kilometers, also called quasi-linear mesoscale convective systems. These systems are associated with extreme weather conditions, including extreme rainfall rates. To better understand and therefore predict this high impact phenomenon, this study investigates the physical processes leading to enhanced precipitation rates when clouds are organized into squall lines, using idealized high-resolution simulations. Interestingly, the dynamics of squall lines, notably their wind structures, are found to play a key role in setting the intensity of extreme rainfall rates.

1. Introduction

In the tropics, the organization of deep convection at mesoscales (i.e., hundreds of kilometers) is ubiquitous, and these mesoscale convective systems (MCSs) plays a major role in producing heavy precipitation (Mathon et al., 2002; Nesbitt et al., 2006; Semie & Bony, 2020). In particular, long-lived MCSs, such as squall lines, contribute disproportionally to extreme tropical precipitation (Roca & Fiolleau, 2020). Understanding the physical mechanisms behind the formation of these systems, as well as those that lead to rainfall extremes, is an important step toward improving prediction models for extreme events.

The key ingredient in squall line formation is the presence of cold pools under precipitating clouds. These are areas of cold air with a negative buoyancy anomaly, driven by partial evaporation of rain and concomitant latent cooling, and have been described to extend from 10 to 200 km in diameter (Romps & Jeevanjee, 2016; Zuidema et al., 2017). Cold pools propagate at the surface as gravity currents, and thus can promote upward motion and the development of new deep convective cells at their edge, as described in Tompkins (2001), and can impact convective aggregation (C. Muller & Bony, 2015; Jensen et al., 2022).

Most of the time, squall lines arise when cold pools interact with a background vertical wind shear. Using idealized cloud-resolving simulations, Robe and Emanuel (2001) show that depending on the intensity of the imposed shear, squall lines tend to orient themselves with respect to the direction of the wind shear. For weak to medium intensity of shear, squall lines are perpendicular to the wind shear direction. For larger shear, squall lines are oriented at an angle with respect to the shear. The orientation aims at restoring a vorticity balance between

Investigation: Sophie Abramian, Caroline Muller, Camille Risi
Methodology: Sophie Abramian, Caroline Muller, Camille Risi
Resources: Caroline Muller
Supervision: Caroline Muller, Camille Risi
Visualization: Sophie Abramian
Writing – original draft: Sophie Abramian
Writing – review & editing: Sophie Abramian, Caroline Muller, Camille Risi

the environmental shear and the cold pool propagation, as predicted by Robe and Emanuel (2001), Rotunno et al. (1988), Bryan and Rotunno (2014), and verified in Abramian et al. (2022). The existence of an optimal balance between shear and cold pools thus makes it possible to define three regimes of squall line development: the suboptimal regime, where the environmental shear is weaker than the shear induced by cold pool spreading; the optimal regime, where equilibrium between environmental shear and cold pools is reached; and the superoptimal regime, where the shear wins, and where the squall lines orient themselves at an angle to the shear, so that the shear projected perpendicular to the squall line is at equilibrium with cold pools (see Figure 1 adapted from Abramian et al. (2022)). A recent study (Mulholland et al., 2021) has also shown that entrainment is reduced in the optimal shear regime, leading to more buoyant and intense updrafts. However, the implication of these regimes for extreme precipitation rates remains poorly documented. A natural question that we address here is then: Are precipitation extremes intensified in suboptimal, optimal or superoptimal squall lines, and if so, why?

More precisely, to answer these questions, a theoretical scaling for precipitation extremes is used, first introduced in Betts (1987) and O'Gorman and Schneider (2009), and refined to link it to microphysics in C. Muller and Takayabu (2020) and C. J. Muller et al. (2011). We draw the attention of the reader on that we focus on small-scale local extreme precipitation that depends on local processes, rather than mean precipitation which generally depends on larger scale and energy budgets (O'Gorman & Muller, 2010). We expect organization to impact both short-time hourly and long-time daily precipitation extremes (Bao & Sherwood, 2019; Da Silva et al., 2021), but these can come from different physical processes. This study focuses on hourly precipitation. The aforementioned scaling allows one to decompose changes in precipitation extremes into three contributions: a thermodynamic contribution related to water vapor, a dynamic contribution related to vertical mass flux in updrafts, and a microphysical contribution related to precipitation efficiency.

With warming, idealized simulations often predict an increase of precipitation extremes following the thermodynamic component in disorganized convection (C. Muller & Takayabu, 2020; C. J. Muller et al., 2011; Romps, 2011). But the thermodynamic contribution is not always the dominant term when ice and mixed-phase processes are important (Singh & O'Gorman, 2014) or when comparing disorganized and organized convection at a given temperature. Recent works (Bao & Sherwood, 2019; Da Silva et al., 2021) show that the microphysical contribution may contribute significantly to the increase of extreme precipitation rates in self-aggregated convection relative to non-aggregated convection (C. Muller et al., 2022). The objective here is to apply this methodology on a set of simulations of squall lines in a cloud-resolving model (CRM), and attempt to answer three questions:

- How do the precipitation extremes evolve with the suboptimal, optimal and superoptimal organization of squall lines? Notably, in the superoptimal regime, how does the orientation of squall lines impact extreme rainfall rates?
- Which contribution mainly explains the response of extreme rainfall rates to squall line organization? Is it the thermodynamic, the dynamic, or the microphysical contribution?
- What physical mechanisms control the behavior of these contributions?

The next section (Section 2) describes the CRM and introduce the theoretical scaling. Extreme precipitation rates, as well as the thermodynamic, dynamic and microphysical contributions, in the suboptimal, optimal and superoptimal squall lines are analyzed in Section 3. We then provide a physical interpretation for all these contribution changes with increasing shear in Section 4. Conclusions, as well as key implications of our results, are discussed in Section 5.

2. Methodology

In this section, we describe the model and simulations (Section 2.1), introduce the theoretical scaling used to analyze contributions to precipitation extremes (Section 2.2), and describe in detail how extremes and contributions are computed from the simulations outputs (Section 2.3).

2.1. Model and Simulations

The simulations use the CRM SAM (Khairoutdinov & Randall, 2003). The setup is the same as Abramian et al. (2022), namely the resolution is 1 km in both horizontal directions (Although 1 km may not be sufficient to

resolve details of cold pools, it is sufficient to capture the interaction of cold pools with shear, and the generation of squall lines (Abramian et al., 2022; C. J. Muller, 2013). A recent study Weisman et al. (2022) shows that 1 km resolution well captures reflectivity characteristics and the smaller leading-line mesoscale vortices compared to 3 km), and gradually increases in the vertical direction from 80 m near the surface to 400 m above 6 km. The 3D domain is doubly periodic in *x* and *y* with 128 km side, and the upper third of the domain (18–27 km) has a sponge layer to absorb gravity waves. Therefore, only the troposphere is simulated in our experiments. We neglect the Earth rotation (a reasonable approximation for mesoscales in the tropics), and there is no diurnal cycle; we use an imposed radiative profile constant in space and time, obtained as the mean equilibrium profile of a shear-free simulation (which used the radiation code from the National Center for Atmospheric Research Community Atmosphere Model). The sea surface temperature is fixed and equal to a value of 300 K. The advection scheme used is MPDATA (following Abramian et al. (2022)). All simulations are run to radiative-convective equilibrium (reached in about 30 days), after which we start our analysis, from day 30 to day 35, with hourly outputs (all variables used in this paper are hourly mean outputs).

Following C. J. Muller (2013) and Abramian et al. (2022), the convection is organized into squall lines by imposing a background vertical wind shear profile in the *x*-direction, with a background wind decreasing linearly from U_{sfc} at the surface to 0 m/s at $z = 1$ km. It is imposed by relaxing the domain-mean wind to the target profile with a time scale of 2 hr. We perform nine simulations, with different shear strengths, that is, with different surface wind U_{sfc} from 0 (no shear) to 20 m/s, with 2.5 m/s increments. The range of shear strength allows three regimes of development for squall lines (again following C. J. Muller (2013) and Abramian et al. (2022)) and is supported by the estimation of the optimal shear in Rotunno et al. (1988) (see Section 4; Equation 9). The case without shear $U_{sfc} = 0$ m/s is very similar to $U_{sfc} = 2.5$ m/s, so we do not discuss it further and define 2.5 m/s as our control case. To avoid an impact of this imposed surface wind on surface fluxes, the domain-mean surface wind is removed before computing surface fluxes (see Section S1 in Supporting Information S1 for more details on the simulations and settings).

Figure 1 shows three of our simulations ($U_{sfc} = 2.5$ m/s, $U_{sfc} = 10$ m/s and $U_{sfc} = 20$ m/s). On the top, we can see 3D graphs representing buoyancy fields on the ground and clouds in white. On the bottom, the 2D graphs also display the buoyancy fields, with the vertical velocity at 500 hPa exceeding 2 m/s in white. In $U_{sfc} = 2.5$ m/s, no organization is observed; as mentioned above, this constitutes our control case. For $U = 10$ m/s we observe strong squall lines, with a typical horizontal scale of 100 km. Consistent with Abramian et al. (2022), the squall lines are typically perpendicular to the wind direction for $U_{sfc} = 10$ m/s (angle $a = 0$ with respect to the *y*-axis), while squall lines are oriented at an angle $a > 0$ for $U_{sfc} = 20$ m/s. This angle preserves the normal shear (orange arrow Figure 1f) near optimal value, that is, such that $U_{sfc} \cos(a) = U_{sfc,opt}$.

2.2. Theoretical Scaling for Precipitation

As mentioned in the introduction, our study of extreme precipitation in squall lines is based on a theoretical scaling that allows to decompose extreme precipitation into three contributions: a thermodynamic contribution related to water vapor, a dynamic contribution related to the vertical mass flux in extreme updrafts and a microphysical contribution related to the precipitation efficiency. The latter is defined as the fraction of condensation in a convective updraft that finally reaches the surface as precipitation. It is generally less than one because some of the condensates are either advected away as clouds, or evaporate as they fall into the unsaturated air below the cloud before reaching the surface. Each of these three contributions is subject to different theoretical constraints, and may respond differently to the imposed shear cases of squall lines. An overview of the origin of this theoretical scale is provided in C. Muller and Takayabu (2020). Although it was first derived using an energy budget, this scaling can be interpreted in terms of the water budget. This allows, under certain approximations (notably the weak horizontal temperature gradient), to relate the precipitation to the condensation rate, with a precipitation efficiency factor, which as mentioned above represents the fraction of condensates that reach the ground as surface precipitation. This scaling can be written as follows

$$P \sim \epsilon\, C \sim \epsilon \int_0^{H_t} \rho w \frac{-\partial q_{sat}}{\partial z} dz \qquad (1)$$

where *P* is the precipitation, *C* is the condensation rate, ϵ the precipitation efficiency, H_t the top of the troposphere (because the vertical domains only extends up to 18 km), ρ the density, *w* the vertical velocity, q_{sat} the saturated
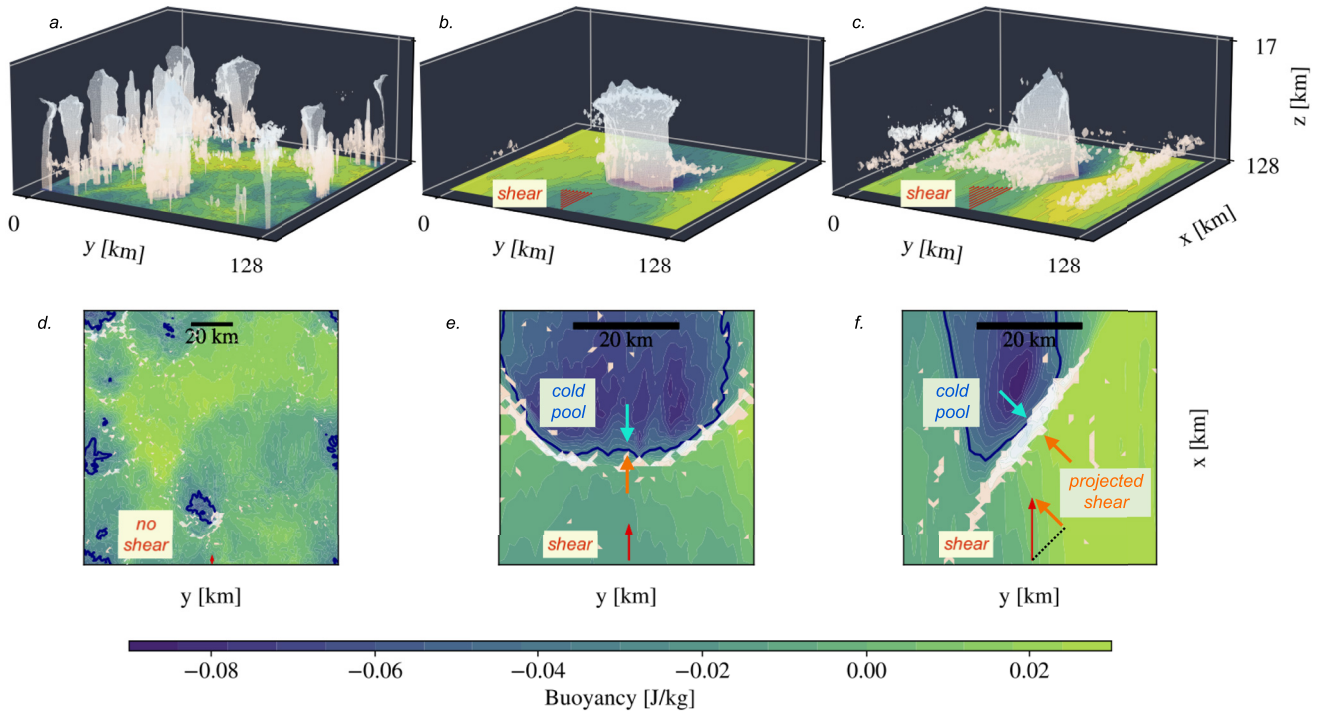
Figure 1. (top) 3D graphs for three simulation cases (U_{sfc} = 2.5 m/s, U_{sfc} = 10 m/s and U_{sfc} = 20 m/s), the buoyancy field is displayed on the ground (integrated to the first atmospheric level) and clouds are in white. The imposed wind is represented by red arrows. As the vertical shear of this horizontal wind increases, the simulations move from a disorganized case to an optimal and then superoptimal squall line. (bottom) Buoyancy field surrounded by high value of mid-tropospheric vertical velocity in white, zoomed near a convective zone to highlight the interaction between wind shear and cold pool spreading at the edge of cold pools in the optimal and superoptimal regimes.

specific humidity and z the altitude. Following Da Silva et al. (2021), the precipitation efficiency is estimated as a residual, and is thus computed as the quotient of the condensation rates over the precipitation rates. More generally, the detailed computation of each term in the simulations will be described in Section 2.3. But before, we describe how this theoretical scaling is used to compare precipitation extremes between different simulations with different shears.

Indeed, in our study, we are more specifically addressing the variations of precipitation extremes P in squall lines compared to an unorganized case $\overline{P}$ (U_{sfc} = 2.5 m/s). We therefore apply the scaling to the relative change in precipitation

$$\frac{\Delta P}{\overline{P}} = \frac{P - \overline{P}}{\overline{P}},$$

and similarly, $\Delta \epsilon / \overline{\epsilon}$ and $\Delta C / \overline{C}$ denote relative changes with respect to the unorganized case U_{sfc} = 2.5 m/s. Based on Equation 1, similarly to a logarithmic derivative, we can express $\Delta P / \overline{P}$ as a function of $\Delta \epsilon / \overline{\epsilon}$ and $\Delta C / \overline{C}$ which leads to:

$$\frac{\Delta P}{\overline{P}} = \frac{\Delta \epsilon}{\overline{\epsilon}} + \frac{\Delta C}{\overline{C}} + \frac{\Delta \epsilon}{\overline{\epsilon}} \frac{\Delta C}{\overline{C}}. \tag{2}$$

Neglecting the second order terms finally gives

$$\frac{\Delta P}{\overline{P}} \sim \frac{\Delta \epsilon}{\overline{\epsilon}} + \frac{\Delta C}{\overline{C}}. \tag{3}$$

At this stage, the condensation rate can be split into two contributions. Indeed, a variation of the condensation rate can be explained either by a stronger vertical advection leading to more condensation for a given saturation profile, this is the dynamic contribution; or by saturation decreasing faster also producing more condensation for a given advection. This further decomposition can be written as

$$\frac{\Delta C}{\overline{C}} \sim \underbrace{\frac{1}{\overline{C}} \int_0^{H_t} \Delta \rho w \frac{-\partial \overline{q_{sat}}}{\partial z} dz}_{dynamic} + \underbrace{\frac{1}{\overline{C}} \int_0^{H_t} \overline{\rho w} \Delta \frac{-\partial q_{sat}}{\partial z} dz}_{thermodynamic} \tag{4}$$

where overbars denote values of the unorganized case and Δ is the difference compared to the control case. We check that second order terms can be neglected (see Supporting Information S1 for more details).

Finally,

$$\frac{\Delta P}{\overline{P}} \sim \frac{\Delta \epsilon}{\overline{\epsilon}} + \underbrace{\frac{1}{\overline{C}} \int_0^{H_t} \Delta \rho w \frac{-\partial \overline{q_{sat}}}{\partial z} dz}_{\frac{\Delta dyn}{\overline{C}}} + \underbrace{\frac{1}{\overline{C}} \int_0^{H_t} \overline{\rho w} \Delta \frac{-\partial q_{sat}}{\partial z} dz}_{\frac{\Delta therm}{\overline{C}}}. \tag{5}$$

Hereafter, the relative dynamic and thermodynamic contributions will be respectively called $\frac{\Delta dyn}{\overline{C}}$ and $\frac{\Delta therm}{\overline{C}}$.

2.3. Evaluation of Extremes of Precipitation, Condensation, and Other Contributions in Simulations

In our study, we define extreme precipitation as the tails of the distribution of hourly mean precipitation (including zeros). More precisely we investigate the response of high precipitation percentiles to the increasing shear. We investigate various percentiles around the 99.9th precipitation percentile (extreme of hourly precipitation occurring 0.1% of the time), and whether this extreme rain rate increases with the squall line organization, and if so why.

One difficulty in evaluating the various terms of Equation 5 is that different extremes occur at different times and locations during the cloud life cycle. Indeed, one expects maximum condensation early in the life cycle of a cloud, and maximum precipitation at the end of the life cycle, as condensation leads to precipitation. To avoid this problem, we follow Singh and O'Gorman (2014) and Da Silva et al. (2021) and compute the terms not at a given point in space and time, but at a fixed percentile rank. In other words, we compute precipitation extremes at a given precipitation percentile, and condensation extremes at a given condensation percentile, without regard to space and time. The precipitation efficiency is deduced from these two extremes and is thus interpreted as an effective efficiency defined as the fraction of extreme condensation that become extreme precipitation on the ground,

$$\left(\frac{\Delta P}{\overline{P}}\right)^{99.9} \sim \left(\frac{\Delta \epsilon}{\overline{\epsilon}}\right)^{99.9} + \left(\frac{\Delta C}{\overline{C}}\right)^{99.9}. \tag{6}$$

The underlying assumption is that an extreme in condensation leads to an extreme in precipitation of similar percentile rank, which is equivalent to an ergodicity hypothesis. To motivate this hypothesis, Figure 2 shows the precipitable water field of the simulation case $U_{sfc} = 10$ m/s for three successive time steps. We observe a squall line developing perpendicular to the wind. The red crosses represent the condensation extremes, that is, the points for which condensation is greater than 99.9th percentile, and the green crosses represent the precipitation extremes. We notice (a) the extremes of precipitation and condensation do not coincide in space at each time step, and (b) the extremes of condensation anticipate the extremes of rainfall, and thus account for the same convective event. This figure shows that if we consider the locations of condensation and precipitation extremes, everything happens as if we were following a cell through its life cycle. The theoretical scaling therefore remains consistent at each percentile rank. A more detailed statistical analysis (Section S2 and Figure S1 in Supporting Information S1) confirms that for high percentiles, precipitation and condensation are strongly correlated in space and time.

Extremes of condensation are decomposed according to Equation 4 into a dynamic and a thermodynamic contribution, both evaluated at extremes of condensation following Da Silva et al. (2021); in other words, the vertical mass flux and saturation specific humidity profiles are computed at condensation extremes. Similarly the precipitation efficiency will be decomposed into a term involving the conversion of non precipitating cloud condensate into precipitating condensate and a term involving the fraction of the precipitating condensate that arrives at the surface as precipitation (α and β respectively in Equation 9, the physical interpretation of these terms will be discussed in more detail in Section 4.2) following Lutsko and Cronin (2018). This computation involves the microphysical flux Q_p of non precipitating condensates into precipitating ones (unit of kg m^{-2} s^{-1}). This
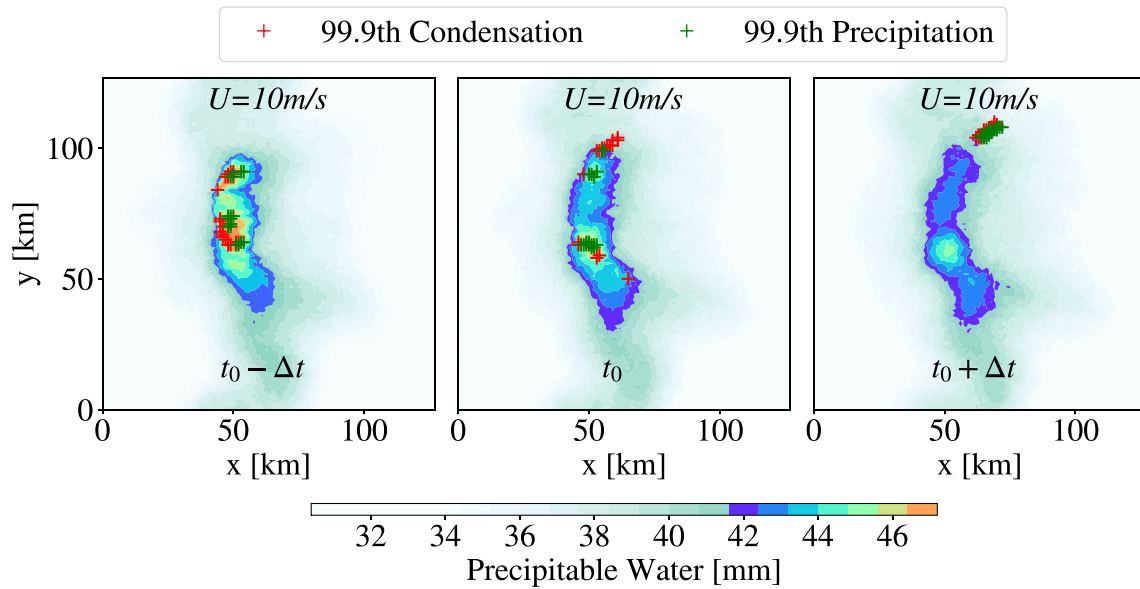
Figure 2. Precipitable Water field of an optimal squall line (U_{sfc} = 10 m/s) displayed for three consecutive time steps (hourly). The red crosses are the extremes of condensation extremes (taken at 99.9th) and green ones are the precipitation extremes (at 99.9th too). This figure underlines (1) extremes of condensation and precipitation are shifted in time and space; (2) condensation extremes anticipate precipitation extremes.

variable is directly output from the model at the same frequency as precipitation and other variables (hourly mean outputs). Each term is evaluated at its own extreme that is, P, C, and Q_p are evaluated at the 99.9th percentile of P, C, and Q_p respectively. Here again we use the hypothesis that consequential events in the life cycle of a convective cell are linked together in their own extreme rank of percentile (an extreme of condensation C leads to an extreme of precipitating condensate production Q_p, which itself leads to an extreme of surface precipitation P).

3. Results: How do Precipitation Extremes Evolve With the Shear in Tropical Squall Lines? Which Contributions of the Scaling Explain This Change?

3.1. Evolution of Precipitation Extremes

Figure 3 shows results from our different simulations with increasing wind shear. As noted in the introduction and in Section 2.1, the orientation of the squall lines aims at restoring the balance between cold pool and the imposed shear perpendicular to the squall lines (see Figure 1). Consistently, we recover the three regimes of Abramian et al. (2022).

In the suboptimal regime (green background), the vorticity of the imposed shear is weaker than that of cold pools. The squall line is perpendicular to the imposed shear (angle $a = 0$ between the squall line and the y axis), which optimizes the projected shear. The projected shear thus increases linearly until the optimal case. The optimal regime (blue background) is found around $U_{sfc,opt} \approx 11$ m/s in our simulations; we note in passing that the projected shear is slightly weaker than the target shear to which we relax the mean wind profile. Indeed, the domain-mean wind is slightly weaker than the imposed target wind profile due to drag and subgrid-scale momentum flux, which oppose the relaxation toward the target profile. In this regime, the incoming shear balances cold pools. In the superoptimal regime (yellow), the shear is higher than the optimal value, and the lines orient themselves at an angle $a > 0$ in order to reduce the projected incoming shear $U_{sfc} \cos(a)$. This angle conserves the projected shear near optimal value, so that the projected shear remains approximately constant above $U_{sfc} \cos(a) = U_{sfc,opt}$.

If we superimpose the extreme precipitation—99.9th percentile of precipitation - for each case, we obtain the green curve. In the disorganized case, $U_{sfc} = 2.5$ m/s, the extreme is 450 mm/day and increases almost linearly as the shear increases, reaching 650 mm/day in the optimal regime. In the superoptimal regime, the rainfall extreme is observed to be constant around 575 mm/day, slightly below the rate at optimal shear.

Panel b shows the change of precipitation extremes relative to the control case for different percentiles (indicated by the colorbar) as a function of the shear. Quantitatively, there is an increase in extreme precipitation of about 30%–40% in the optimal regime relative to the control case, and it declines in the superoptimal regime but is
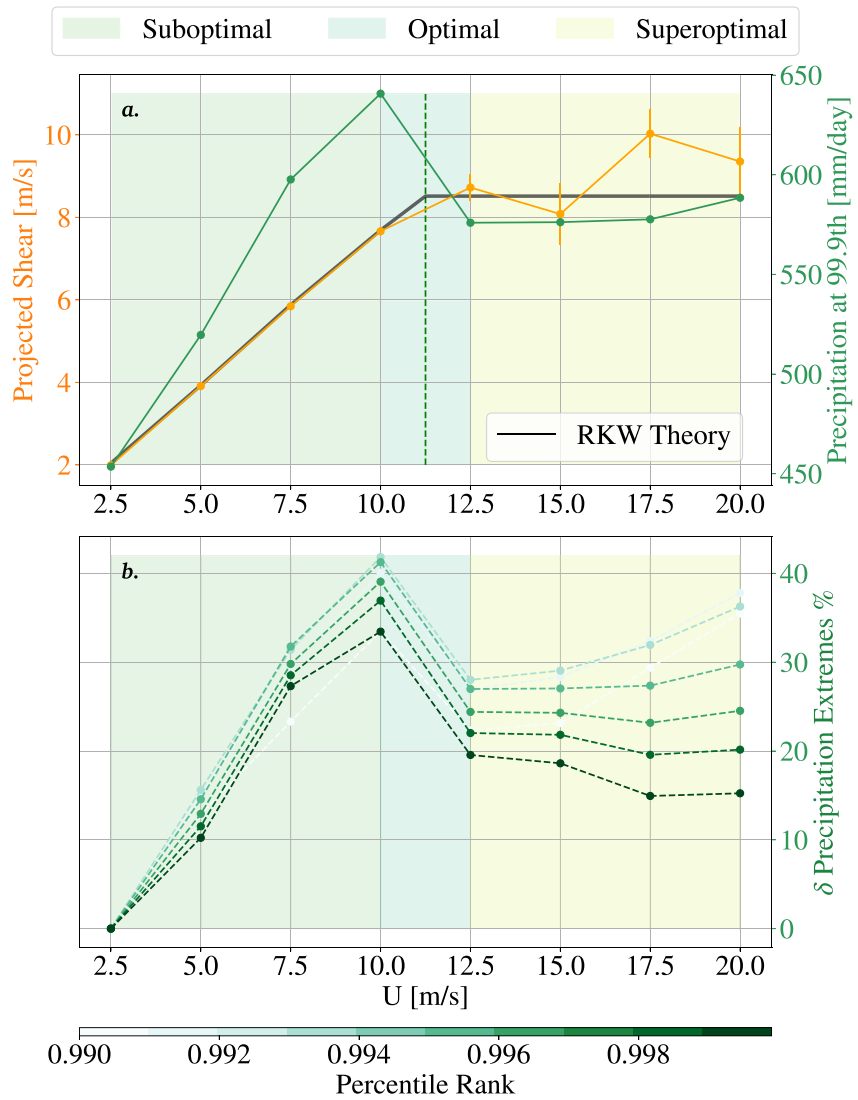
Figure 3. (a) Superposition of the incoming wind shear on squall lines for all simulation cases (orange, near-surface wind projected in the direction perpendicular to the squall line) and the respective extreme precipitation rate taken at 99.9th percentile (green). The black line represents the theoretical value of the projected wind (described in Rotunno et al. (1988), and described in more detailed in Abramian et al. (2022) Section 3.2) and we observe a very good agreement with the measured one, consistent with Abramian et al. (2022). In dashed green the optimal case is highlighted, around 11 m/s, and allows to identify the three regimes of development: sub-optimal (light green), the optimal (light blue) and the superoptimal (light yellow). This figure demonstrates the sensitivity of extreme precipitation to the regime of squall lines. (b) Changes in precipitation per percentile rank, from 99th to 99.99th. Values of extremes are calculated relative to the control case (U_{sfc} = 2.5 m/s). Extremes increase by 30%–40% in the optimal case, and remain 20%–30% higher in the superoptimal case. The trend of extremes with squall lines regime is robust to the percentile.

maintained around 20%–30%, again relative to the control case. The signal is robust to the chosen definition of extreme; from now on, we will only show results at the 99.9th percentile.

The focus of the present study shall be to understand what controls this evolution of precipitation extremes with squall lines organization, and what physical mechanisms are involved.

3.2. Results of the Scaling

Figure 4 shows the various contributions from the scaling (Equations 4 and 5) in each simulation. We have displayed the value of the extremes (99.9%) of precipitation for each simulation in green, the extremes of condensation
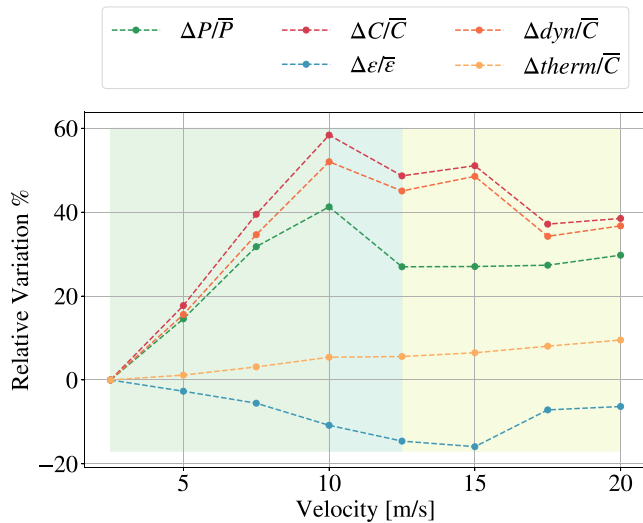
Figure 4. Relative sensitivity to shear of precipitation extremes $\left(\frac{\Delta P}{\overline{P}}\right)$ and its decomposition into dynamic $\left(\frac{\Delta dyn}{\overline{C}}\right)$, thermodynamic $\left(\frac{\Delta thermo}{\overline{C}}\right)$ and microphysical $\left(\frac{\Delta \varepsilon}{\overline{\varepsilon}}\right)$ components using the scaling for all simulations (see Equation 5). The 99.9th percentile of precipitation is in dashed green, the 99.9th percentile of condensation rate is in dashed red, itself decomposed into the dynamic (orange) and thermodynamic (yellow) contributions; the microphysics contribution is in dashed blue. The values of extremes are displayed relative to the control case ($U_{sfc} = 2.5$ m/s). For example, in the optimal case, $U_{sfc} = 10$ m/s, the increase of 40% of precipitation is due to an increase in 60% in condensation, of which 55% of dynamics and 5% of thermodynamics, and by a decrease of 15% in microphysics. Over all cases, the change in precipitation are due first to dynamics, then to microphysics and eventually to thermodynamics.

in red and the efficiency of precipitation in blue. The thermodynamic and dynamic contributions are shown in light and dark orange respectively (both taken at extreme condensation columns as described in Section 2.3).

This decomposition indicates for instance that for the case $U_{sfc} = 10$ m/s, the increase in precipitation extremes of 40% is due to an increase in condensation of 60% and a decrease in precipitation efficiency of about 15% (the residual difference is due to higher order terms neglected in Equation 2). Overall, in all the simulations, the variations in the condensation rate explain the variations in precipitation. Focusing on the two contributions, dynamic and thermodynamic, we notice, still for the case $U_{sfc} = 10$ m/s, that when condensation increases by 60%, this is due to an increase of 50% in dynamics, and 10% in thermodynamics. More generally, in all the simulations, the dominant contribution to changes in extreme precipitation is the dynamic contribution. In Section 4, we investigate the physical processes at play.
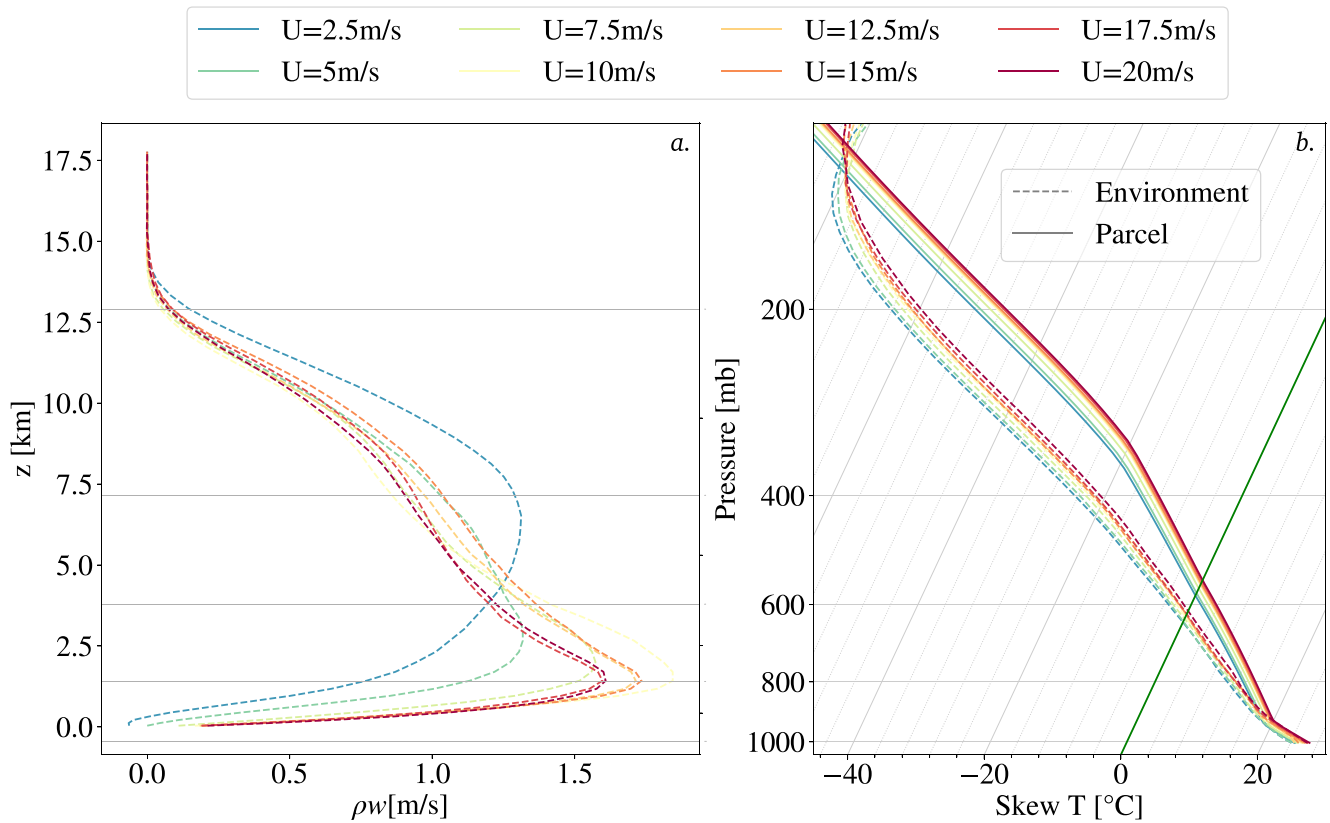
4. What Physical Mechanisms Control the Behavior of These Contributions?

4.1. Dynamics Driven by Cloud-Base Updraft Velocity

Figure 5a shows the mass flux profiles at condensation extremes. In this figure, we note that as the shear increases, the profile changes from a parabolic shape, for $U_{sfc} = 2.5$ m/s, to a so-called "bottom heavy" profile. Quantitatively, the value of w in the low troposphere, for instance at 2 km, increases until the 10 m/s case, and then decreases. This trend is maintained throughout the lower layer, and in particular at the top of the boundary layer (around 1 km).

In order to further investigate vertical velocities, we look at the change of atmospheric instability as measured by CAPE. Figure 5b shows the temperature profiles of a parcel in an adiabatic lift (solid lines), as well as the temperature of the environment (dashed line) on a SkewT diagram. These profiles are calculated at the extremes of the pointwise, vertically-integrated CAPE, because we assume that extremes of condensation rates follow extremes of CAPE (see Section S3 in Supporting Information S1 for details of the CAPE computation). In this diagram, the CAPE is read as the area between the parcel and the environmental profile, since we neglect virtual effect.

CAPE seems to be insensitive to shear, since both the domain and parcel warm at a similar rate as the shear is increased, keeping the CAPE constant between cases (see Figure 5b). We note in passing that organization is accompanied by warming, consistent with C. J. Muller and Held (2012) and Bretherton et al. (2005). This suggests that the increased dynamic contribution with shear is not related to atmospheric instability as measured by CAPE (acceleration of the parcel as it moves upward). However, what can indeed play a non negligible role is the fraction of conversion of CAPE into kinetic energy, which can vary with imposed shear, and depends on entrainment processes. This quantity can be estimated as a residual of the acceleration of an undiluted parcel ascent and the vertical velocity profiles from our simulation outputs (captured by the conversion factor λ in Equation 7 below). Qualitatively, we expect the conversion fraction to increase with organization, since the entrained air in organized convection is moister and has a lower dilution effect, as has been described in the literature (Becker et al., 2018; Feng et al., 2015; Mulholland et al., 2021). On the basis of these studies, entrainment is expected to play a dominant role in modifying the conversion rate, but other processes may also contribute, such as condensate loading. Further work is needed to fully assess these effects.

We argue that the change in the dynamics are not only due to the change in CAPE conversion, but may also be related to the cloud-base velocity (initial velocity of the upward moving parcel at the top of the boundary layer). Intuitively, this is also consistent with the bottom heavy profiles of mass flux in Figure 5. We further investigate this assumption with a conservation of energy, written as

$$w^2(z) = w_{cb}^2 + 2\lambda(z)\text{CAPE}(z) \tag{7}$$

Figure 5. (a) Mass flux profiles (ρw) for all cases, computed for high condensate columns (beyond 99.9th). The control case (U_{sfc} = 2.5 m/s), in blue, is a near parabolic profil, and as the shear increases we observe profiles becoming more "bottom heavy," consistant with Abbott et al. (2020). The mass flux at the boundary layer increase until the optimal regime and slowly decrease in the superoptimal regime. (b) Environment temperature profile, averaged near an extreme of CAPE (beyond 99.9th) in dashed lines, and adiabatic parcel ascent in solid lines are displayed in Skew-T diagrams. The CAPE for each case is read as the area between two profiles of same color. This graph highlights the low sensitivity of the CAPE to shear changes across simulation experiments.

where $w(z)$ denotes the vertical velocity at altitude z, w_{cb} is the cloud-base ($\sim$1 km) updraft velocity, CAPE(z) the convective available potential energy between the first level of the atmosphere and the level z and $\lambda(z)$ the conversion fraction, computed as a residual. (This budget implicitly neglects the contributions to vertical velocity from viscosity and from pressure perturbations.) This equation can be interpreted as the decomposition into a cloud-base initial updraft velocity, and a term that reflects the acceleration above cloud-base due to the instability of the atmosphere. Taking differential with respect to the control case yields

$$\Delta w = \underbrace{\frac{\overline{w_{cb}}\Delta w_{cb}}{\overline{w}}}_{\Delta cb/\overline{w}} + \underbrace{\frac{\overline{\lambda}\Delta\text{CAPE}}{\overline{w}}}_{\Delta pe/\overline{w}} + \underbrace{\frac{\overline{\text{CAPE}}\Delta\lambda}{\overline{w}}}_{\Delta ent/\overline{w}},$$

(8)

where Δ refers to a difference to the control case (2.5 m/s), overlined quantities are taken at the control case, w, λ are defined above, and cb, pe, ent correspond to cloud-base, potential energy and entrainment respectively. We calculate this decomposition to quantify the role of cloud-base updraft vertical velocity, CAPE and dilution in changing the dynamics (using Equation 8 in the integral of the dynamical term in Equation 5). The cloud-base updraft velocity w_{cb} is computed as the vertical velocity at 1 km at locations of extreme condensation (Figure 5a). Δw is calculated at each level, and is then weighted by the saturation specific humidity profiles to be consistent with the dynamical contribution. Its increase, as well as the other terms in Equation 8, are quantified in Figure 6. The evolution of the dynamic contribution is in dashed dark orange (repeated from Figure 4 to ease comparison), and the three dynamic sub-contributions, the convective cloud-base updraft velocity, the atmospheric instability and the conversion fraction, are represented respectively in solid orange, brown and yellow. This figure shows the dominant roles of the cloud-base velocity that initiates convective updraft and the conversion fraction in the
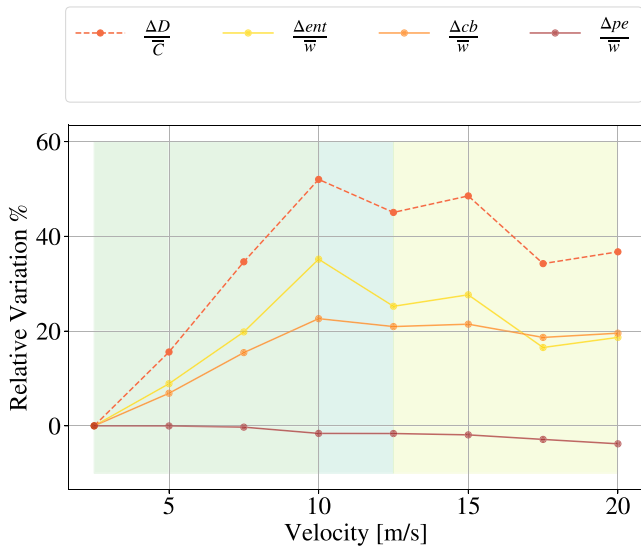
Figure 6. Decomposition of the dynamic contribution (dashed dark orange $\Delta D/\overline{C}$) into a cloud-base velocity term (solid orange $\Delta cb/\overline{C}$), an atmospheric instability term (solid brown $\Delta pe/\overline{C}$) and the conversion rate (solid yellow, $\Delta ent/\overline{C}$) for all simulation cases. The cloud-base velocity and the conversion term dominate the change in dynamic contribution.

dynamic variation with shear. As mentioned above, we expect the conversion fraction to follow the degree of organization of squall lines, and consistently it increases in the suboptimal and optimal regime, and then reaches a plateau.

What is more unexpected is that the cloud-base velocity is also found to saturate in the superoptimal regime (Figure 6). The cloud-base updraft velocity may then only depend on the balance of the projected horizontal shear and the cold pool spreading. This is apparently what suggests Figure 7. The panels on the left show the surface winds at extreme condensation rate, where we see that the horizontal wind is perturbed as it crosses the cold pool, and in the superoptimal case, we observe that the excess momentum in the incoming shear is removed in the direction tangential to the squall line. In both cases, we find that the circulation is more complex than the simple picture of the cold pool spreading at equilibrium with the incoming shear; indeed, part of the horizontal wind is found to make it through the cold pool, and only the converging fraction into the black rectangle is expected to contribute to the vertical cloud base initial velocity. When we look at anomaly of horizontal wind instead, shown in the right panels, we find the expected low-level convergence. In these cross sections, horizontal wind anomalies are displayed on top of the buoyancy field, both composited at extreme condensation rate. The cloud-base updraft velocity results from the convergence in the horizontal plane below 1 km and probably encapsulates the effects of the pressure perturbation that deflects the incoming horizontal flow into the vertical direction.

To quantify this further, we compute a mass balance at the edge of the cold pool, in the reference frame of the squall line (black rectangles Figure 7). The reference frame is aligned with the squall line and since the lines are oriented at an angle a as the shear increases, the frame of reference is also rotated. We consider a volume centered at maximum condensation, with angle $a = 0$ to the y-axis in the suboptimal and optimal squall lines, and angle
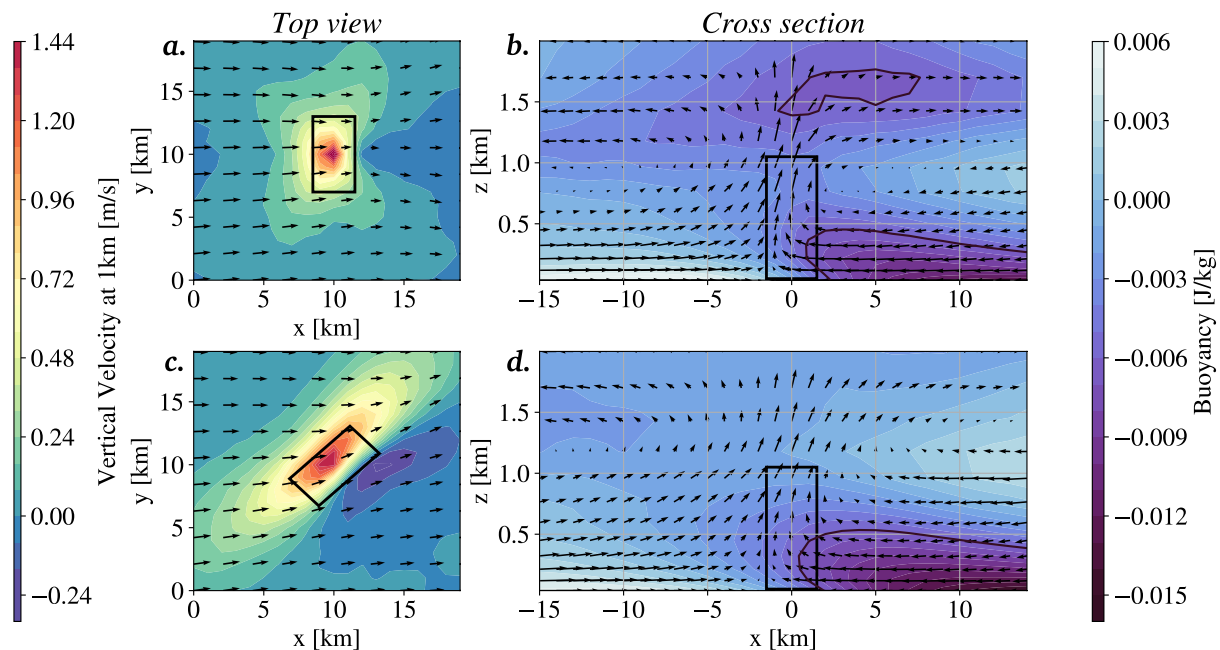
Figure 7. Vertical velocity maps at 1 km height and buoyancy cross section fields for two cases, 12.5 and 20 m/s are displayed. These fields are composited near the extreme of condensation (99.9th). Horizontal velocity anomaly, at 1 km too, are displayed in quiver in the top view. We observe stronger updraft in organized cases (12.5 and 20 m/s), with a subsidence zone. This figure also highlights the orientation of the line in the superoptimal regime. For the cross section, the quiver represent the incoming flow both from the shear and the cold pool. We compute the mass balance in a volume represented by the black rectangle, in order to deduce the strength of the convective cloud-base updraft velocity at 1 km.
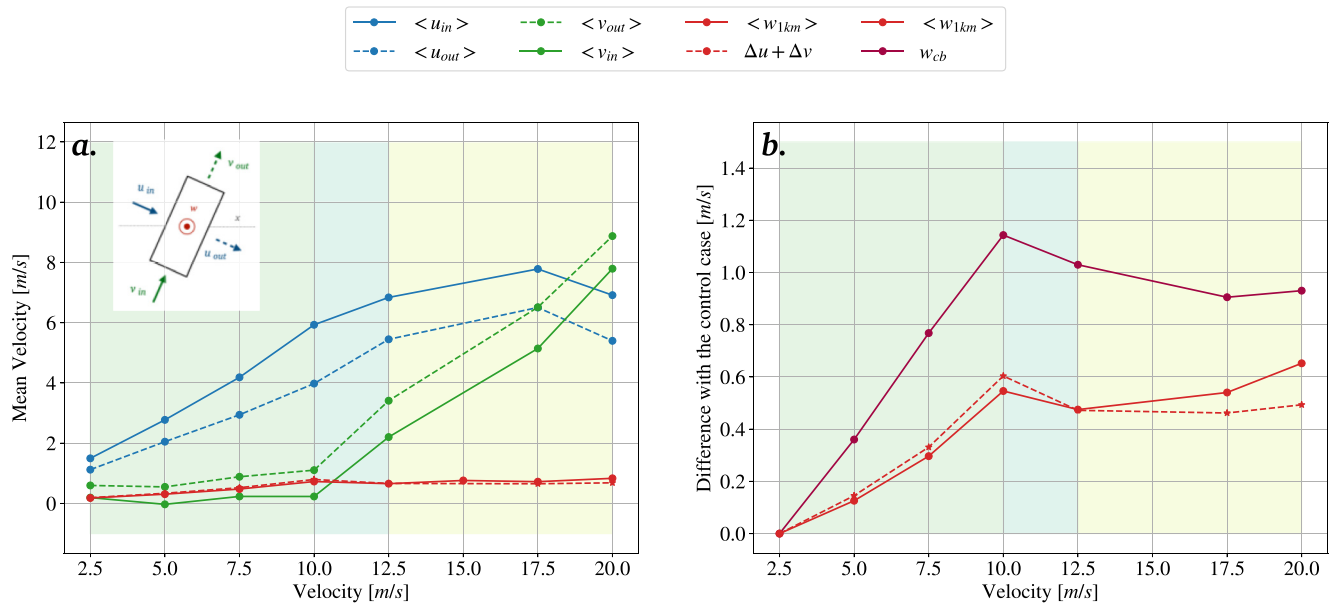
Figure 8. (a) The inflow (solid line) and outflow (dashed) in the perpendicular (blue) and parallel (green) direction of the squall line, as well as the outflow at the top of the volume (red) are shown for each experiments (the inset shows the rectangle repeated from Figure 7 with notations). We observe the saturation of the perpendicular component from the optimal case, as well as the increase of the tangential component, which supports our initial hypothesis. (b) Relative evolution of the mean cloud base velocity (red) compared to the one of the cloud base updraft velocity at extremes of condensation (purple). The variations of these two quantities are coherent and support our approach of modeling the cloud base velocity at extremes of condensation with the mean value of vertical velocity obtained from a mass balance. (The case $U = 15$ m/s has a changing propagation from increasing y to decreasing y which distorts the composites and has thus been removed in parallel and perpendicular estimates).

$a > 0$ increasing in the superoptimal squall lines consistent with its orientation (i.e., such that $U_{sfc} \cos(a) = U_{sfc,opt}$, see Figure 1). The rectangular volume has length $L = 6$ km parallel to the squall line, width $l = 1.5$ km across the line, and height $H = 1$ km.

Mass balance decomposition in the rectangle of Figure 7 is displayed in Figure 8a. In blue, the incoming and outgoing horizontal winds perpendicular to the squall line are displayed ($<u_{in}>$ and $<u_{out}>$, where $<.>$ denotes averaging over the rectangle sides). We observe that as the shear increases, the net incoming wind $\Delta u = <u_{in} - u_{out}>$ increases, until the optimal shear is reached, and then the difference remains constant. In green, the increase of the tangential components ($<v_{in}>$ and $<v_{out}>$) in the superoptimal regime is clear. This supports that the exceeding momentum in the incoming shear in the superoptimal squall lines is removed in the direction tangential to the squall line. However the net incoming ($\Delta v = <v_{in} - v_{out}>$) slightly increases until the optimal shear is reached, and then remains approximately constant in the superoptimal regime. As a consequence, the convergence $\Delta u + \Delta v$ increases until the optimal case, and then saturates (dashed red), consistent with the mean velocity at the top of the volume at 1 km $<w_{1km}>$ (solid red) as expected from mass balance (the small difference is due to interpolation approximation near the rectangle). We notice that the value of the vertical velocity is almost 10 times smaller than the horizontal velocities, and this is explained by the mean flow passing through the cold pool. Investigating what controls the mean flow intensity and how it is related to the imposed wind shear would provide a theoretical scaling for the mean cloud-base velocity. We can hypothesize a dependence to the projected shear, but more work is needed to answer this question.

Figure 8b compares the evolution of the difference with the control case of the cloud-base updraft velocity (w_{cb} from Equation 7), and the mean cloud-base velocity at the top of the rectangular volume (same as in Figure 8a). Both evolutions are similar, except that the mean velocity is lower, due to the effect of averaging. This suggests that the cloud-base updraft velocity variation results from those of the convergence in the horizontal plane, itself controlled by the orientation of the squall line, which removes exceeding momentum of the incoming shear into the tangential direction.

Thus, to leading order, precipitation extremes follow the dynamical contribution, itself dictated by the change of conversion fraction and the cloud-base updraft velocity at the top of the boundary layer, which follow the degree
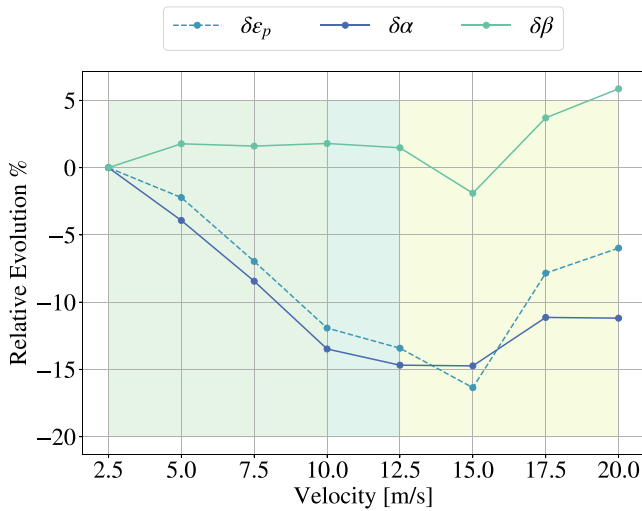
Figure 9. Decomposition of the precipitation efficiency (dashed blue) into a sedimentation term (green) and a conversion (blue) for all cases. The decrease in microphysics contribution is mainly explained by the decrease in conversion.

of organization, and consequently the regime of development of squall lines. The change of conversion of CAPE with organization is consistent with the literature (Becker et al., 2018; Feng et al., 2015; Mulholland et al., 2021), and is in our opinion an interesting impact of organization which would deserve further investigation. The change in initial cloud-base velocity of updrafts is also an important aspect in our squall lines. We explain this phenomenon with the increased winds perpendicular to the squall line in the suboptimal and optimal regimes. The saturation in the superoptimal regime is due to the squall line orientation, which maintains the projected wind perpendicular to the squall line close to its optimal value. The rest of the paper is now devoted to the other, smaller thermodynamic and microphysical contributions.

4.2. Microphysical Component Driven by Conversion Rate

The change of precipitation efficiency reaches about -15% in the optimal and -5% in the superoptimal simulations (Figure 4). In order to further investigate this change in precipitation efficiency, we follow Lutsko and Cronin (2018) and split the precipitation efficiency ϵ into two terms. The first term α is the rate of conversion from cloud to precipitating condensates Q_p (in kg m^{-2} s^{-1}), normalized by the rate of conversion from water vapor to cloud condensate C. It captures how efficiently cloud condensates are converted into precipitating condensates. Therefore, α is called conversion efficiency (Lutsko & Cronin, 2018). The second term, $(1 - \beta)$, referred to as sedimentation efficiency (Lutsko & Cronin, 2018), represents the fraction of source of precipitating condensate (Q_p) from microphysics which reaches the ground as surface precipitation (P). This fraction is typically less than unity because a fraction β of rain evaporates as precipitating condensates fall through subsaturated air. The microphysical variable Q_p is diagnosed directly from the model, and those two terms are computed using the following:

$$\epsilon \sim \frac{P}{C} \sim \underbrace{\frac{Q_p}{C}}_{\alpha} \times \underbrace{\frac{P}{Q_p}}_{1-\beta}. \tag{9}$$

Figure 9 represents the relative variations of the precipitation efficiency, the conversion and the sedimentation in the different simulations. We observe that changes in precipitation efficiency are mainly driven by changes in conversion. Further investigation (see Section S4; Figures S2 and S3 in Supporting Information S1), decomposing α into contributions from accretion and auto-conversion, shows that the decrease of conversion is mainly due to a decrease of accretion. Intuitively, this suggests that the stronger updraft causes more cloud condensate due to not enough time for the auto-conversion process in the optimal and super-optimal balance experiments.

### 4.3. Thermodynamical Component Driven by Change in Surface Humidity

The objective of this sub-section is to understand the origin of the small increase of the thermodynamic contribution, which increases by 10% in the $U = 20$ m/s case compared to the control case. The thermodynamic contribution is written

$$\frac{1}{\overline{C}} \int_0^{H_t} \overline{\rho w} \Delta \left(\frac{-\partial q_{sat}}{\partial z} \right) dz. \tag{10}$$

We can approximate this contribution as

$$\frac{1}{\overline{C}} \int \overline{\rho w} \Delta \left(\frac{-\partial q_{sat}}{\partial z} \right) dz \sim \frac{1}{\overline{C}} \overline{\rho w}_{500hPa} \Delta \int \frac{-\partial q_{sat}}{\partial z} dz = \frac{1}{\overline{C}} \overline{\rho w}_{500hPa} \Delta \left(q_{sat}^{sfc} \right). \tag{11}$$

This equation yields an approximate relationship between the thermodynamic component and surface saturation humidity. As the temperature increases when a stronger shear wind is imposed (Figure 5b), this leads to an increase in the saturation humidity at the surface. This increase can therefore explain the changes in thermodynamic
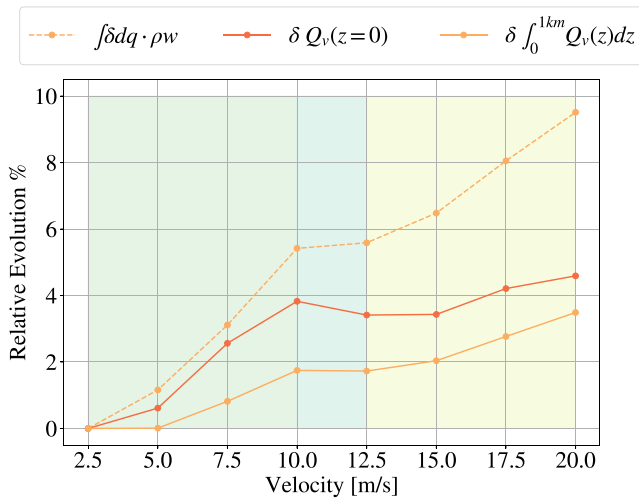
Figure 10. Comparison between the thermodynamic contribution (dashed yellow) and a simplified scaling, taking into account the change of humidity at saturation at the surface (solid orange), and the change integrated in the boundary layer (solid yellow). This figure shows that out of 10% of thermodynamic increase, almost half is due to near surface changes.

contribution. We have plotted in Figure 10 the variation of the saturation humidity at the surface (solid red line), as well as over the whole height of the boundary layer (solid orange) to compare them to the total thermodynamic contribution (dashed orange). This figure shows that out of 10% of thermodynamic increase, almost half is due to surface changes. As noted above, Equation 11 is an approximate relation between the thermodynamic component and near-surface saturation humidity. So quantitatively, we do not expect a perfect agreement, but qualitatively, the thermodynamic contribution increase is consistent with the humidity increase.

5. Conclusion

Squall lines, and more generally organized convection, are associated with extreme weather conditions, notably extreme rainfall rates. Here, we investigate in idealized cloud-resolving simulations, the physical origin of the amplification of precipitation extremes in squall lines. We also clarify how this amplification varies in the suboptimal, optimal and superoptimal squall line regimes. These regimes are obtained in the simulations by increasing low-level shear following Abramian et al. (2022). We find that precipitation extremes are sensitive to the squall line regime and most notably to their orientation with respect to the shear. We observe a gradual increase of precipitation extremes in the suboptimal regime, up to a 30%–40% increase in the optimal regime. This increase saturates at 20%–30% in the superoptimal regime.

To understand these changes, we use a theoretical scaling, described in C. Muller and Takayabu (2020), which estimates the precipitation as the amount of water that condenses through vertical advection in updrafts, multiplied by a precipitation efficiency. This efficiency takes into account the part of the water that remains in the clouds, and the droplets that re-evaporate into the subsaturated air. The particularity of our method is to consider this scaling statistically true at each percentile rank rather than at a specific point in space (following Da Silva et al. (2021)), to account for the cloud life cycle (an extreme of condensation in the early stage of a cloud leads to an extreme in precipitation at a later stage). Using this method, we are able to identify that the increase in precipitation extremes is due to an increase in condensation rates with imposed shear. More precisely, we show that the dynamic component is mainly responsible for the condensation increase. The microphysical contribution plays a secondary, but not negligible, damping role. The thermodynamic contribution is the weakest.

We also focus on the physical mechanisms at the origin of these variations. For the dynamical contribution, we show that it is the effect of dilution by entrainment and the cloud-base updraft velocity of the convective cells between cases that are most important. The former is consistent with reduced effective entrainment with organization, as updrafts in organized convection are surrounded by moister air. The latter is explained by the fact that the orientation, by re-establishing the equilibrium between cold pools and incoming shear, acts to maintain constant the cloud-base velocity that initiates convective updrafts. This is what differentiates the suboptimal regime where precipitation extremes increase with shear, from the optimal and superoptimal regimes preventing further increase of extremes in superoptimal squall lines. For the microphysical component, conversion rates are lower in the optimal regime presumably because the conversion of non-precipitating hydrometeors to rain is slower than the condensation of water vapor into non-precipitating hydrometeors. Finally, the thermodynamic component seems to increase with near-surface humidity which is sensitive to the increase in temperature with shear.

These results should draw our attention to the consequences of the organization of convection, and in particular its sensitivity to temperature increase. The 40% increase in optimal squall lines are larger than the thermodynamic increase in extremes associated with a 3 K warming expected from the Clausius-Clapeyron equation (7%/K increase). These results highlight the need to understand changes in the organization of convection, especially in the context of global warming. Changes in organization have a potentially more severe effect on rainfall extremes than warming. Over Sahel, where observations indicate the leading role of large MCSs in explaining the trends in extreme precipitation, recent convection-permitting climate model simulations highlight tropospheric

wind shear changes as the primary reason for intensifying squall lines under warming conditions (Fitzpatrick et al., 2020). Extending our idealized simulation results to more realistic data would be desirable, to better understand changing organization and implications for precipitation extremes. The global cloud-resolving simulations of the Dyamond/Next-GEMS project (Stevens et al., 2019) could be useful tools to address this important scientific question. Observations of surface properties at fine-scale resolution (kilometers, notably within cold pools), such as those proposed in the ESA Harmony mission (Earth Explorer 10 mission), will be crucial to perfect our understanding of the interaction between cold pools, shear and precipitation extremes (Harmony, 2020).

Data Availability Statement

The simulation data that support the findings are available from the Irene server of the TGCC (Very Large Computing Center) of the CEA (Atomic Energy Center), and can be found in Figshare (https://doi.org/10.6084/m9.figshare.21360396.v1). The different algorithms and the main script developed in this article are freely available on the Zenodo SAM project repository (https://doi.org/10.5281/zenodo.7225550), including the pySAM Python package with a new release (see also Section S5 in Supporting Information S1).

References

Abbott, T. H., Cronin, T. W., & Beucler, T. (2020). Convective dynamics and the response of precipitation extremes to warming in radiative–convective equilibrium. *Journal of the Atmospheric Sciences*, *77*(5), 1637–1660. https://doi.org/10.1175/jas-d-19-0197.1

Abramian, S., Muller, C., & Risi, C. (2022). Shear-convection interactions and orientation of tropical squall lines. *Geophysical Research Letters*, *49*(1), e2021GL095184. https://doi.org/10.1029/2021gl095184

Bao, J., & Sherwood, S. C. (2019). The role of convective self-aggregation in extreme instantaneous versus daily precipitation. *Journal of Advances in Modeling Earth Systems*, *11*(1), 19–33. https://doi.org/10.1029/2018ms001503

Becker, T., Bretherton, C. S., Hohenegger, C., & Stevens, B. (2018). Estimating bulk entrainment with unaggregated and aggregated convection. *Geophysical Research Letters*, *45*(1), 455–462. https://doi.org/10.1002/2017gl076640

Betts, A. K., & Harshvardhan (1987). Thermodynamic constraint on the cloud liquid water feedback in climate models. *Journal of Geophysical Research*, *92*(D7), 8483–8485. https://doi.org/10.1029/jd092id07p08483

Bretherton, C. S., Blossey, P. N., & Khairoutdinov, M. (2005). An energy-balance analysis of deep convective self-aggregation above uniform SST. *Journal of the Atmospheric Sciences*, *62*(12), 4273–4292. https://doi.org/10.1175/jas3614.1

Bryan, G. H., & Rotunno, R. (2014). The optimal state for gravity currents in shear. *Journal of the Atmospheric Sciences*, *71*(1), 448–468. https://doi.org/10.1175/jas-d-13-0156.1

Da Silva, N. A., Muller, C., Shamekh, S., & Fildier, B. (2021). Significant amplification of instantaneous extreme precipitation with convective self-aggregation. *Journal of Advances in Modeling Earth Systems*, *13*(11), e2021MS002607. https://doi.org/10.1029/2021ms002607

Feng, Z., Hagos, S., Rowe, A. K., Burleyson, C. D., Martini, M. N., & de Szoeke, S. P. (2015). Mechanisms of convective cloud organization by cold pools over tropical warm ocean during the AMIE/DYNAMO field campaign. *Journal of Advances in Modeling Earth Systems*, *7*(2), 357–381. https://doi.org/10.1002/2014ms000384

Fitzpatrick, R. G., Parker, D. J., Marsham, J. H., Rowell, D. P., Guichard, F. M., Taylor, C. M., et al. (2020). What drives the intensification of mesoscale convective systems over the West African Sahel under climate change? *Journal of Climate*, *33*(8), 3151–3172. https://doi.org/10.1175/jcli-d-19-0380.1

Harmony. (2020). Harmony Mission Description. Retrieved from https://esamultimedia.esa.int/docs/EarthObservation/EE10_Harmony_Report-for-Assessment-v1.0_13Nov2020.pdf

Jensen, G. G., Fiévet, R., & Haerter, J. O. (2022). The diurnal path to persistent convective self-aggregation. *Journal of Advances in Modeling Earth Systems*, *14*(5), e2021MS002923. https://doi.org/10.1029/2021ms002923

Khairoutdinov, M. F., & Randall, D. A. (2003). Cloud resolving modeling of the ARM summer 1997 IOP: Model formulation, results, uncertainties, and sensitivities. *Journal of the Atmospheric Sciences*, *60*(4), 607–625. https://doi.org/10.1175/1520-0469(2003)060<0607:crmota>2.0.co;2

Lutsko, N. J., & Cronin, T. W. (2018). Increase in precipitation efficiency with surface warming in radiative-convective equilibrium. *Journal of Advances in Modeling Earth Systems*, *10*(11), 2992–3010. https://doi.org/10.1029/2018ms001482

Mathon, V., Laurent, H., & Lebel, T. (2002). Mesoscale convective system rainfall in the Sahel. *Journal of Applied Meteorology*, *41*(11), 1081–1092. https://doi.org/10.1175/1520-0450(2002)041<1081:mcsrit>2.0.co;2

Mulholland, J. P., Peters, J. M., & Morrison, H. (2021). How does vertical wind shear influence entrainment in squall lines? *Journal of the Atmospheric Sciences*, *78*(6), 1931–1946. https://doi.org/10.1175/jas-d-20-0299.1

Muller, C., & Bony, S. (2015). What favors convective aggregation and why? *Geophysical Research Letters*, *42*(13), 5626–5634. https://doi.org/10.1002/2015gl064260

Muller, C., & Takayabu, Y. (2020). Response of precipitation extremes to warming: What have we learned from theory and idealized cloud-resolving simulations, and what remains to be learned? *Environmental Research Letters*, *15*(3), 035001. https://doi.org/10.1088/1748-9326/ab7130

Muller, C., Yang, D., Craig, G., Cronin, T., Fildier, B., Haerter, J. O., et al. (2022). Spontaneous aggregation of convective storms. *Annual Review of Fluid Mechanics*, *54*(1), 133–157. https://doi.org/10.1146/annurev-fluid-022421-011319

Muller, C. J. (2013). Impact of convective organization on the response of tropical precipitation extremes to warming. *Journal of Climate*, *26*(14), 5028–5043. https://doi.org/10.1175/jcli-d-12-00655.1

Muller, C. J., & Held, I. M. (2012). Detailed investigation of the self-aggregation of convection in cloud-resolving simulations. *Journal of the Atmospheric Sciences*, *69*(8), 2551–2565. https://doi.org/10.1175/jas-d-11-0257.1

Muller, C. J., O'Gorman, P. A., & Back, L. E. (2011). Intensification of precipitation extremes with warming in a cloud-resolving model. *Journal of Climate*, *24*(11), 2784–2800. https://doi.org/10.1175/2011jcli3876.1

Nesbitt, S. W., Cifelli, R., & Rutledge, S. A. (2006). Storm morphology and rainfall characteristics of TRMM precipitation features. *Monthly Weather Review*, *134*(10), 2702–2721. https://doi.org/10.1175/mwr3200.1

O'Gorman, P., & Muller, C. J. (2010). How closely do changes in surface and column water vapor follow Clausius–Clapeyron scaling in climate change simulations? *Environmental Research Letters*, *5*(2), 025207. https://doi.org/10.1088/1748-9326/5/2/025207

O'Gorman, P. A., & Schneider, T. (2009). Scaling of precipitation extremes over a wide range of climates simulated with an idealized GCM. *Journal of Climate*, *22*(21), 5676–5685. https://doi.org/10.1175/2009jcli2701.1

Robe, F. R., & Emanuel, K. A. (2001). The effect of vertical wind shear on radiative-convective equilibrium states. *Journal of the Atmospheric Sciences*, *58*(11), 1427–1445. https://doi.org/10.1175/1520-0469(2001)058<1427:teovws>2.0.co;2

Roca, R., & Fiolleau, T. (2020). Extreme precipitation in the tropics is closely associated with long-lived convective systems. *Communications Earth & Environment*, *1*(1), 18. https://doi.org/10.1038/s43247-020-00015-4

Romps, D. M. (2011). Response of tropical precipitation to global warming. *Journal of the Atmospheric Sciences*, *68*(1), 123–138. https://doi.org/10.1175/2010jas3542.1

Romps, D. M., & Jeevanjee, N. (2016). On the sizes and lifetimes of cold pools. *Quarterly Journal of the Royal Meteorological Society*, *142*(696), 1517–1527. https://doi.org/10.1002/qj.2754

Rotunno, R., Klemp, J. B., & Weisman, M. L. (1988). A theory for strong, long-lived squall lines. *Journal of the Atmospheric Sciences*, *45*(3), 463–485. https://doi.org/10.1175/1520-0469(1988)045<0463:atfsll>2.0.co;2

Semie, A. G., & Bony, S. (2020). Relationship between precipitation extremes and convective organization inferred from satellite observations. *Geophysical Research Letters*, *47*(9), e2019GL086927. https://doi.org/10.1029/2019gl086927

Singh, M. S., & O'Gorman, P. A. (2014). Influence of microphysics on the scaling of precipitation extremes with temperature. *Geophysical Research Letters*, *41*(16), 6037–6044. https://doi.org/10.1002/2014gl061222

Stevens, B., Satoh, M., Auger, L., Biercamp, J., Bretherton, C. S., Chen, X., et al. (2019). DYAMOND: The DYnamics of the Atmospheric general circulation Modeled On Non-hydrostatic Domains. *Progress in Earth and Planetary Science*, *6*(1), 61. https://doi.org/10.1186/s40645-019-0304-z

Tompkins, A. M. (2001). Organization of tropical convection in low vertical wind shears: The role of cold pools. *Journal of the Atmospheric Sciences*, *58*(13), 1650–1672. https://doi.org/10.1175/1520-0469(2001)058<1650:ootcil>2.0.co;2

Weisman, M. L., Manning, K. W., Sobash, R. A., & Schwartz, C. S. (2022). Simulations of severe convective systems using 1- versus 3-km grid spacing. *Weather and Forecasting*, *38*(3), 401–423. https://doi.org/10.1175/waf-d-22-0112.1

Zuidema, P., Torri, G., Muller, C., & Chandra, A. (2017). Precipitation-induced atmospheric cold pools over oceans and their interactions with the larger-scale environment. *Surveys in Geophysics*, *38*(6), 1283–1305. https://doi.org/10.1007/s10712-017-9447-x

References From the Supporting Information

Fildier, B., Parishani, H., & Collins, W. (2018). Prognostic power of extreme rainfall scaling formulas across space and time scales. *Journal of Advances in Modeling Earth Systems*, *10*(12), 3252–3267. https://doi.org/10.1029/2018MS001462

Lin, Y.-L., Farley, R. D., & Orville, H. D. (1983). Bulk parameterization of the snow field in a cloud model. *Journal of Applied Meteorology and Climatology*, *22*(6), 1065–1092.